Article

Size-Dependent Properties of Solution-Processable Conductive MOF Nanocrystals

Checkers R. Marshall, Josh P. Dvorak, Liam P. Twight, Lan Chen, Kentaro Kadota, Anastasia B. Andreeva, Alexandra E. Overland, Thomas Ericson, Anthony F. Cozzolino, and Carl K. Brozek*

Read Online

ACCESS | 📊 Metrics & More | 📖 Article Recommendations | 🗾 Supporting Information

ABSTRACT: The diverse optical, magnetic, and electronic behaviors of most colloidal semiconductor nanocrystals emerge from materials with limited structural and elemental compositions. Conductive metal−organic frameworks (MOFs) possess rich compositions with complex architectures but remain unexplored as nanocrystals, hindering their incorporation into scalable devices. Here, we report the controllable synthesis of conductive MOF nanoparticles based on $Fe(1,2,3\text{-triazolate})_2$. Sizes can be tuned to as small as 5.5 nm, ensuring indefinite colloidal stability. These solution-processable MOFs can be analyzed by solution-state spectroscopy and electrochemistry and cast into conductive thin films with excellent uniformity. This unprecedented analysis of MOF materials reveals a strong size dependence in optical and electronic behaviors sensitive to the intrinsic porosity and guest−host interactions of MOFs. These results provide a radical departure from typical MOF characterization, enabling insights into physical properties otherwise impossible with bulk analogues while offering a roadmap for the future of MOF nanoparticle synthesis and device fabrication.

Redox-active MOF colloids

5.5 nm FeTA₂ · 5.5 nm · 130 nm
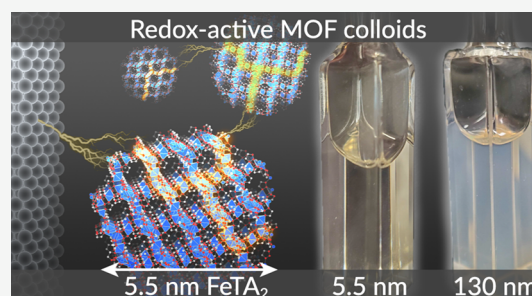
INTRODUCTION

The discovery of colloidal metal and semiconductor nanocrystals has led to a revolution in materials chemistry.[1] While the class of materials known as metal−organic frameworks (MOFs) attracts broad interest due to their highly accessible surface areas and wide synthetic tunability, their preparation as stable, monodisperse nanoparticles remains an open frontier.[2] Nevertheless, recent research into the few examples of MOF nanoparticles has revealed enhanced properties compared to their bulk counterparts due to greater mass transport rates, higher ratios of exposed surface areas, and superior processability, leading to higher catalytic activities, improved gas permeability in separation membranes, more uniform integration into composite films, and utility as unique drug delivery agents.[3−7] The controlled synthesis of MOF nanoparticles with precise sizes will therefore facilitate their application in myriad applications while enabling solution-state analysis to reveal size-dependent physical properties.[8] Currently, the MOFs that can be prepared as colloidally stable nanoparticles with narrow size dispersities[9] are electrical insulators, whereas conductive MOF nanoparticles will enable electronic technologies that benefit from the microporosity and high surface areas of MOFs and the processability and size control of nanoparticles.[10] Here, we address the long-standing challenge of making solution-processable conductive MOF nanoparticles (nanoMOFs) with controlled sizes and narrow dispersity. Solution processability also enables solution-state

spectroscopy for the unprecedented analysis of electronic properties, and thin-film fabrication reveals a unique insight into their redox chemistry and charge transport phenomena.

RESULTS AND DISCUSSION

Size-Tunable Synthesis of Iron Triazolate Nanoparticles. Nanoparticles of $Fe(TA)_2$ (TA = 1,2,3-triazolate) were prepared with tunable sizes by modifying the standard bulk synthesis[11] through addition of 1-methylimidazole (1-mIm) as a "modulator" (Figure 1). Although the use of "modulators," usually monotopic analogues of native MOF linkers,[9] is common in MOF nanoparticle syntheses, their mechanistic role has been debated, especially because increasing modulator equivalents leads to smaller sizes in some systems but larger sizes in others. Previous studies from our laboratory point to a "seesaw" model where modulators impact particle sizes by interfering with linker deprotonation (Figure 1, eq 1) and metal−linker complexation (eq 3). Based on a meta-data analysis of the literature,[9] this model contends that MOF particles result from kinetic trapping of metal ions
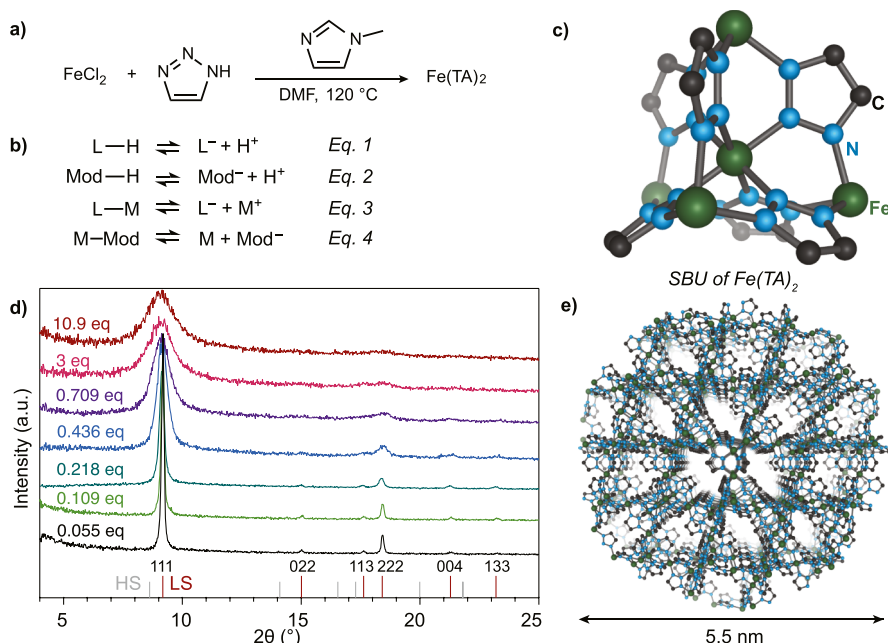
Figure 1. Overview of Fe(TA)$_2$ nanocrystal synthesis. (a) General synthetic route to Fe(TA)$_2$ nanoparticles using 1-mIm as a modulator. (b) Equilibrium between metal ions (M), linkers (L), and modulators (Mod) that control MOF nanoparticle formation. (c) SBU cluster of Fe(TA)$_2$. (d) PXRD patterns of the Fe(TA)$_2$ nanoparticles synthesized with varying amounts of 1-mIm. Red and gray lines indicate expected reflections for the low-spin (LS) phase and high-spin (HS) phase, respectively. (e) Idealized representation of a 5.5 nm Fe(TA)$_2$ particle based on the bulk crystalline structure.
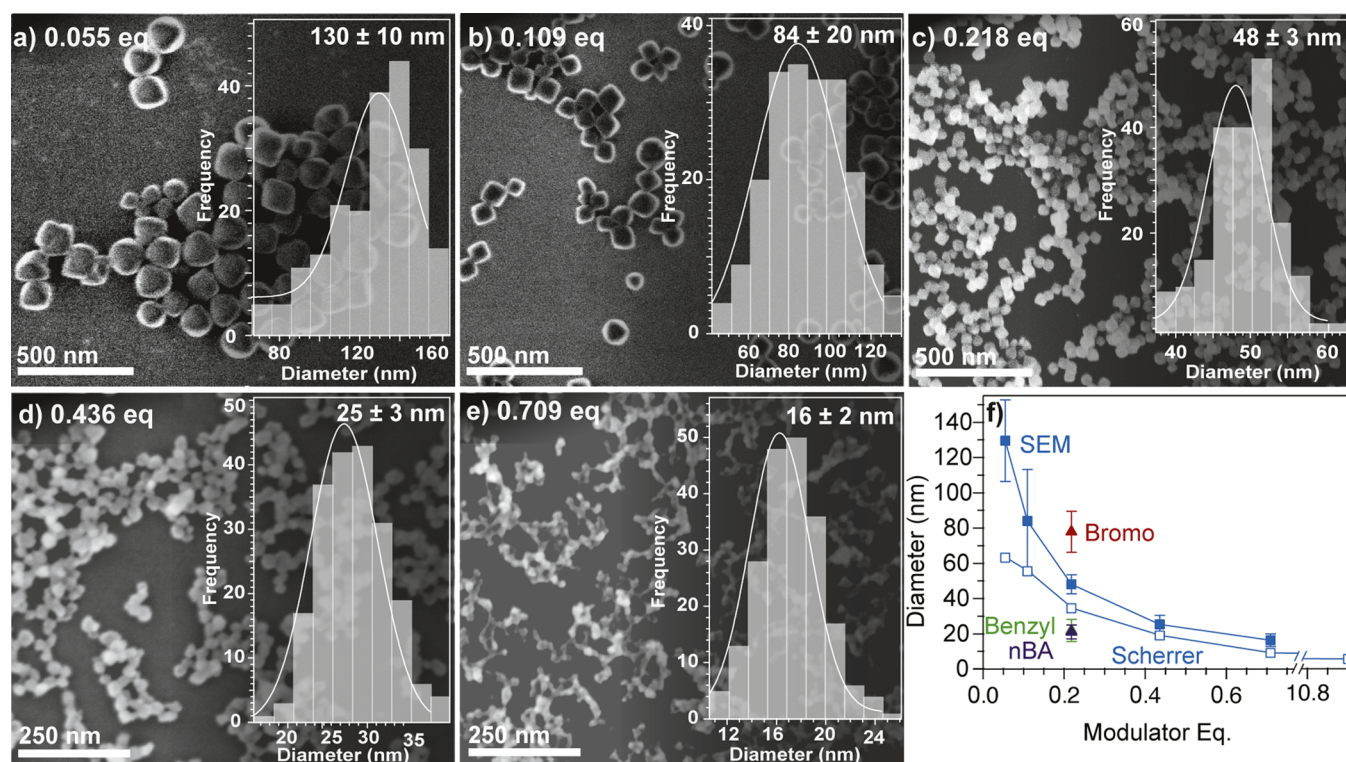
Figure 2. Particle sizes of Fe(TA)$_2$ resulting from modulated syntheses. (a−e) SEM images of Fe(TA)$_2$ nanoparticles synthesized with 1-mIm equivalents (with respect to FeCl$_2$) ranging from 0.055 equiv (a) to 0.709 equiv (e). Images were set to grayscale using Adobe Illustrator. Insets: histograms of particle size distributions from >200 particles fitted to weighted Gaussian distributions. (f) Particle sizes using 1-mIm (blue squares), 1-benzyl-2-methylimidazole (benzyl, green triangle), 5-bromo-1-methylimidazole (bromo, red triangle), and *n*-butylamine (*n*BA, purple triangle). Filled data points were determined by SEM and open data points by Scherrer analysis.

by excess linkers or modulators. Through deliberate control of the key parameters outlined by this model—proton activity, concentration, and ligand excess—excellent size reproducibility can be achieved for benchmark MOF materials.[12] Using these

insights, we can devise MOF syntheses previously inaccessible at the nanoscale. To access small and controllable particle sizes, we hypothesized that a monotopic imidazole linker, 1-mIm, would work as a modulator that mimics the native MOF linker. Reversible bonds between Fe and 1-mIm (eq 4) would compete with metal−linker complexation (eq 3) to rapidly form the secondary building units (SBUs) of $Fe(TA)_2$, shown in Figure 1c. The presence of the monotopic linker at the surface of a growing particle also inhibits further growth until it dissociates. Additionally, previous works with other MOF systems have shown promising nanosizing effects with the use of similar imidazole modulators.[13,24]

In comparison to the bulk synthesis first reported by Yaghi et al.,[11,14,15] the synthesis of nanoparticles was conducted under dilute conditions, with stirring and varying modulator equivalents. After heating the reaction mixture under air-free conditions in dimethylformamide (DMF) at 120 °C, the reaction was terminated after 1.5 h by removing it from heat and immediately centrifuging and washing. These reactions are low yielding (6−23%), which is further evidence of arrested growth of kinetically trapped particles, as has been observed in other nanoMOF systems (Figure S4). Indeed, Figure 1d shows the expected powder X-ray diffraction (PXRD) pattern of $Fe(TA)_2$ but with peaks that broaden with greater equivalents of the modulator. Additionally, Figure 2 shows that particle sizes determined by Scherrer analysis of these data and by scanning electron microscopy (SEM) imaging dramatically decrease with increasing equivalents of 1-mIm. At low equivalents of 1-mIm, the particle sizes decrease steeply: from 0.055 to 0.709 equiv, the particle sizes reduce from 130 to 16 nm. Beyond 0.709 equiv, the particle sizes level off abruptly, decreasing to 5.5 nm only with 10.9 equiv of the modulator (Figures 2f and S5a). To the best of our knowledge, the 5.5 nm particles represent some of the smallest reported MOF particle sizes synthesized by a facile one-pot modulator method, whereas the synthesis of nanoMOFs below 10 nm typically requires multiphase systems, dropwise additions, or multiple modulator ligands.[16−18] Figure 1e depicts a simulated structure of 5.5 nm $Fe(TA)_2$, confirming that such a small size still includes many pores due to the unusually high density of this MOF. SEM analysis of the 16 and 25 nm particles reveals unimodal and symmetrical size distributions and essentially spherical morphologies (Figure 2). Although the two smallest particle sizes synthesized were not well-resolved by SEM, the images clearly reveal small nanoscale particles (Figure S9). Instead, particle sizing was accomplished by Scherrer analysis. To confirm the domain sizes from PXRD, we additionally performed Le Bail refinements on patterns of the largest and smallest particles and found that the domain sizes agree with SEM imaging for the 130 nm particles and Scherrer analysis for the 5.5 nm particles (Table S1 and Figure S6). Scherrer analysis, as expected, produces underestimated values, particularly as particle sizes increase. Microscopy of larger particles (0.055 equiv 1-mIm, 130 nm) shows octahedral faceting, akin to the bulk MOF product. Size distributions also skew toward larger sizes when the modulator equivalents are low, indicating that particles may grow by non-classical mechanisms such as digestive ripening or inter-particle coalescence.[19,20] The dispersity of the particle populations can be quantified from SEM data by dividing the standard deviation given from a Gaussian fit by the mean size; these values vary between 0.09 and 0.18. These dispersity values are considerably lower than the typical dispersity values of

nanoMOFs, which are often as high as 0.6,[21,22] and rival the archetype of low-dispersity MOF particles, ZIF-8, which also exhibits values around 0.09.[23,24,26] Mössbauer spectra of the smallest particles before and after air exposure were collected to determine the efficacy of our air-free synthesis. In the air-free sample, Fe^{3+} is not observed (Figure S15). As the smallest particles exhibit the highest external surface area and would therefore oxidize readily, these data suggest that all samples synthesized, stored, and measured air-free exist in the fully ferrous state. Whereas modulators may incorporate as internal defects or surface ligands in other MOF systems, ^{1}H acid digestion NMR spectroscopy indicates that 1-mIm does not incorporate in most cases (Figure S11). Remarkably, despite the lack of conventional capping ligands, particles of all sizes exhibit colloidal stability in DMF under anaerobic conditions for at least three months, even at relatively high concentrations of 10−20 mg/mL. Dynamic light scattering measurements of 25 nm particles stored for three months gave a solvated diameter of 60 ± 10 nm, a reasonable increase from the SEM images of dried particles that did not exhibit aggregation (Figure S8). Therefore, these $Fe(TA)_2$ particles exhibit superior long-term stability compared to previously reported MOF systems, which, with the notable exception of ZIF-8 in methanol, must be coated with polymers or surfactants to achieve colloidal stability.[22,25]

To explore the general application of this nanocrystal synthetic route, we investigated 5-bromo-1-methylimidazole, 1-benzyl-2-methylimidazole, and *n*-butylamine (*n*BA) as alternatives to 1-mIm. Because of their differences in Lewis and Brønsted−Lowry basicities, this series of modulators offers a platform for exploring the competing equilibria outlined in Figure 1b. Specifically, we expected that *n*BA, as the strongest ligand and proton acceptor, would yield the smallest sizes. Figure 2f plots the resulting particle sizes using 0.218 equiv of each modulator, indicating that each of these alternative modulators produces nanoparticles, with *n*BA giving the smallest sizes and the bromo-substituted variant, that is, the weakest ligand, producing the largest sizes. This trend correlates with the strength of the N−Fe bond as the weakly electron-donating benzyl group allows the imidazole nitrogen to increase its σ-donating ability, whereas the electronegative bromine moiety withdraws electron density from the N−Fe bond. This size trend therefore provides further evidence that modulators compete with the triazole MOF linkers. SEM images confirm that the resulting particles are also uniform (Figure S3), but unlike particles synthesized with 1-mIm, their PXRD patterns indicate minor phase impurities (Figure S1), and accordingly, 1-mIm was selected as the standard modulator for subsequent syntheses. Encouraged by the results with $Fe(TA)_2$, we explored the synthesis of $Co(TA)_2$ with the addition of 1-mIm and observed a similar size trend by Scherrer analysis and SEM imaging (Figure S7). Indeed, this synthetic strategy yielded $Co(TA)_2$ nanoparticles much smaller in size than their Fe-containing analogues, proving that the addition of 1-mIm as a modulator may be a generally applicable method to synthesize nanoMOFs comprising triazole linkers.

Size-Dependent Optical Properties of Colloidal Fe-$(TA)_2$ Nanoparticles. The remarkable colloidal stability and small sizes of $Fe(TA)_2$ nanoparticles yielded suspensions with minimal light scattering, as seen in the inset photograph of Figure 3a. In fact, diluting colloidal suspensions of $Fe(TA)_2$ results in samples with sufficient transparency for solution-state
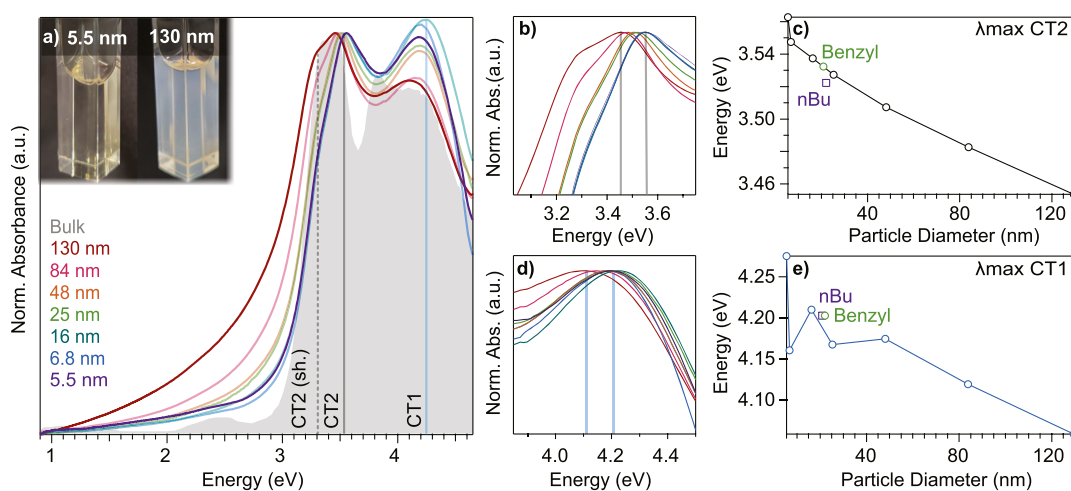
Figure 3. Solution-state UV−vis absorption spectra of $Fe(TA)_2$ nanoparticles. (a) Normalized spectra of colloidal $Fe(TA)_2$ nanoparticles of varying sizes suspended in DMF (colored traces) compared with the bulk MOF (filled gray area) as reported by diffuse reflectance.[14] Smallest and largest particle traces are emphasized. Inset contains a photograph of the smallest and largest particles as solutions in cuvettes. (b) Normalized CT2 band and (c) corresponding peak maxima vs particle sizes. (d) Normalized CT1 band and (e) corresponding peak maxima versus particle sizes. Peak maxima are reported for syntheses modulated by 1-mIm except for data labeled for nBA and 1-benzyl-2-methylimidazole (benzyl).

UV−vis absorption spectroscopy. In general, any spectroscopy of MOF materials involves analysis of solid-state samples, with UV−vis analysis demanding diffuse reflectance methods. Figure 3a shows solution-state UV−vis spectra for all $Fe(TA)_2$ particle sizes. These spectra comprise some of the only examples of solution-state spectroscopy of MOF materials, which include isolated reports of UiO-66, MOF-525, TMU-34, and Zn-MOF-74.[27−30] To the best of our knowledge, this report is the first to quantify fundamental optical properties from the absorbance spectra of MOF particles in solution. The spectra exhibit the same two MLCT bands (ca. 4.2 and 3.3 eV) as observed in the bulk material (Figure 3a, shaded gray). Because of significant scattering observed in the spectra of larger particle sizes, the low-intensity d−d transition expected at 2.36 eV for the LS-state material from the bulk spectrum is obscured in all spectra. Notably, the spectra lack an inter-valence-charge-transfer band around 1.24 eV that arises from mixed $Fe^{2+/3+}$ valency, suggesting that the particles exist in a fully ferrous state, in agreement with the Mössbauer spectra showing only Fe^{2+} (Figure S15).[14]

Close inspection of the solution-state spectra reveals that the peak maxima of the two charge-transfer bands decrease in energy with increasing particle sizes, while a shoulder emerges at energies below the lower-energy band (Figure 3). For the higher energy band (CT1), the maximum shifts a total of 0.22 eV, while the lower band (CT2) maximum shifts 0.11 eV. In the bulk material, the λ_{max} of CT1 appears at a lower energy of 3.99 eV, and CT2 appears at 3.47 eV, within the range of the λ_{max} of the nanoparticles. Although the CT2 band is split in the bulk spectrum, the peak-to-peak separation appears more extreme in the nanoparticles, with the lower-energy shoulder appearing at much lower energies (Figure S18). These data represent the first examples of size-dependent shifts to optical properties of MOF materials. To determine whether the modulator plays a role in the size dependence, UV−vis spectra of particles synthesized with nBA and 1-benzyl-2-methylimi-dazole were collected. Because modulated MOF syntheses often introduce defects, we anticipated the modulator identity to influence the extent of defect incorporation in $Fe(TA)_2$ nanoparticles.[30] Interestingly, the λ_{max} values for particles

prepared with these alternative modulators are similar to $Fe(TA)_2$ particles prepared with 1-mIm. Therefore, the size-dependent optical behavior is unlikely due to modulator-induced defects and is reproducible (Figure 3c,e).

The shift in the peak maxima suggests that the electronic structure of $Fe(TA)_2$ changes with the particle size. Several physical scenarios might explain this observation. The first possibility is quantum confinement; particle sizes smaller than the excitonic Bohr radius of $Fe(TA)_2$ would exhibit blue-shifted absorption events. Previous electronic structure calculations of $Fe(TA)_2$, however, depict relatively shallow band curvatures and therefore low charge-carrier mobilities, which would result in insufficiently large excitonic radii for quantum confinement.[31] Additionally, band-gap transitions of quantum-confined materials linearly increase with $1/r^2$, based on the effective mass approximation, or $1/r$ due to Coulombic electron−hole interactions.[32] However, a linear trend is not observed in this transition with respect to $1/r^2$ or $1/r$ (Figure S20). A second explanation may be that the observed optical shifts arise from a size-dependent magnetic transition. Previous studies of bulk $Fe(TA)_2$ indicate that LS Fe^{2+} centers undergo spin-crossover transitions at 290 °C,[15] but this transition temperature might occur at lower temperatures for smaller particles due to decreased cooperativity of smaller domain sizes. For example, the spin-crossover temperatures of related Fe-based 1-D coordination polymers decrease with decreasing particle sizes.[33] The distinct electronic configurations of HS and LS states would produce different sets of spectra, as is well-documented for spin-crossover materials.[34,35] Preliminary PXRD analysis, however, suggests the nanoparticles exist in the denser LS crystallographic phase (Figure 1d).[15] Addition-ally, we observe by differential scanning calorimetry that the LS−HS phase transition still occurs far above room temper-ature for even the smallest $Fe(TA)_2$ particles (Figure S14). Partial oxidation of iron sites is another possibility, as a change in shape of the charge-transfer bands has been reported for $Fe(TA)_2$ bulk powders after chemical oxidation.[14] This scenario is, however, unlikely as the colloids are stored and measured air-free, the spectra lack an inter-valence charge-transfer band,[14] and Mössbauer spectra of the smallest particles

exhibit only a ferrous species (Figure S15). Finally, structural distortions due to the high surface-to-volume ratios of small particles could be responsible for the size-dependent spectral shifts as optical shifts arising from surface restructuring have been reported in several metal-oxide nanoparticle systems.[36] Specifically, the localized orbitals of surface, sub-surface, and internal species in different geometries could contribute different absorption bands to the UV–vis profile, with surface species playing the greatest role in the smallest particles. Delocalized wavefunctions, on the other hand, might respond coherently to structural distortions, contorting the shapes of valence band and conduction band orbitals and shifting their relative energies. The presence of surface defects is supported by N_2 sorption experiments, which show that the 48 nm particles display a lower accessible surface area than the bulk material despite their higher surface area-to-volume ratio (Figure S10). This strong size dependence in the absorption energies has never before been observed for MOFs. Although the exact cause is yet unknown, we have ruled out several possibilities and are investigating the size dependence further in ongoing studies.

Conventional spectroscopy of bulk MOFs inhibits interpretation of absorption intensities, while solution-state measurements allow for the determination of extinction coefficients (ε) for all $Fe(TA)_2$ particle sizes. The quantitative analysis of extinction coefficients has driven the quantum mechanical understanding of semiconductor nanocrystal optical phenomena by relating optical oscillator strengths (f) to detailed information about the electronic structure and by providing a practical estimation of particle concentrations from optical spectra.[37,38] Such analysis is currently limited for MOF materials and existing reports lack the necessary variable MOF concentrations. To date, only one report discusses the dependence of optical properties—in this case, fluorescence—on the particle size and defectiveness.[30] Figure 4a plots the extinction coefficients of peak maxima versus particle diameters, which increase by 4 orders of magnitude, from 10^6 $(cm^{-1}\ M^{-1})$ for 5.5 nm particles to 10^{10} $(cm^{-1}\ M^{-1})$ for 130 nm particles. Extinction coefficients were determined using a linear relationship between the concentration and extinction at low concentrations, with both absorption and scattering processes contributing to the overall extinction (Figure S19). It is evident from the spectra alone that the extinction coefficients depend strongly on particle sizes, with larger particles absorbing more intensely than smaller particles, as expected from the increased number of absorber units (Figure 4b). To explain this dramatic increase in absorber strength, the extinction coefficient data were fitted to cubic functions of particle diameters, as has been demonstrated for lead chalcogenide semiconductor nanocrystals based on the hypothesis that absorber strength per particle arises from increased particle volumes.[39] A cubic relationship produces an excellent fit except for larger sizes, in which the experimental data appear depressed in relation to the expected cubic trend, most likely due to light scattering (Figure 4a). While greater extinction coefficients may be expected for larger particles, the absorption strength per $Fe(TA)_2$ formula unit depends on particle diameters as well, ranging from ~3000 to 7000 cm^{-1} M^{-1}, which are typical values observed for molecular charge-transfer bands (Figure S18). For a deeper analysis of absorption intensities, the oscillator strength f can be determined for each of the absorption bands. When calculated per particle, f increases with particle size (Figure 4c), as
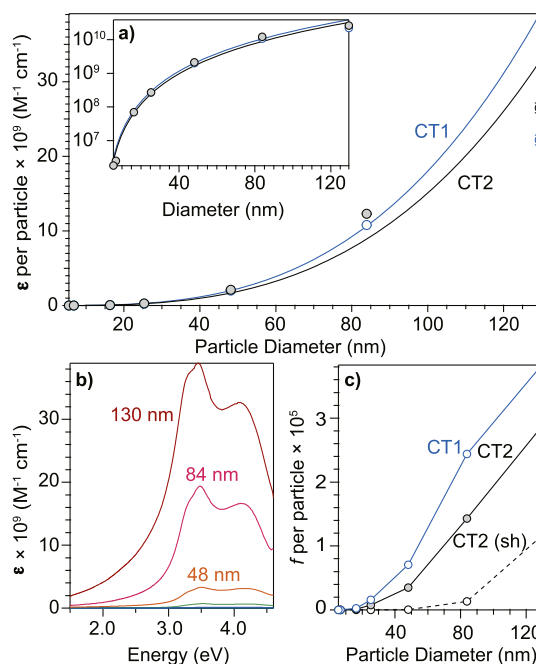

Figure 4. Solution-state UV–vis absorption spectra of $Fe(TA)_2$ nanoparticles. (a) CT1 (blue) and CT2 (black) extinction coefficients plotted as ε per particle vs particle diameter. Solid curves are fits of ε to cubic functions of the diameter. Pre-factors for CT1 and CT2 fits are 18 013 and 15 100, respectively. (b) UV–vis traces for all particle sizes plotted as the extinction coefficient ε per particle. (c) Oscillator strength determined per particle for the two charge-transfer bands as well as the shoulder (sh) of CT2.

expected for an increased number of absorbing units. Determined per formula unit, the oscillator strength changes minimally with particle size, with f values ranging from 0.05 to 0.27 (Figure S21). In all cases, f per formula unit is on the order of 10^{-1}, as expected for a charge transfer that is both spin and parity allowed. Combined, these results show that colloidal stability enables powerful quantitative analysis of the optical properties of MOF nanocrystals. Although the analysis herein does not yet consider possible non-linear contributions of scattering to total extinction, this type of analysis represents a step forward for understanding the optical properties of MOF structures.[40,41]

Size-Dependent Redox Chemistry and Charge Transport of $Fe(TA)_2$ Nanoparticles. Although solid-state techniques and additives such as polymer binders are required to study redox properties of bulk MOFs, the colloidal stability of $Fe(TA)_2$ nanoparticles enables characterization by solution-state electrochemistry. Figure 5a shows cyclic voltammogram (CV) traces for several particle sizes using standard three-electrode cell configurations. These four smallest-sized particles were stable in 0.1 M TBAPF$_6$/DMF electrolyte mixtures under applied bias, while attempts to analyze 48 nm particles failed, likely due to aggregation, as the particles precipitated from the stored electrolyte solution over the course of a few days. Although we expected only a single redox event corresponding to $Fe^{2+/3+}$ oxidation, all samples exhibited qualitatively similar traces with three broad, quasi-reversible features appearing at similar applied potentials. The 16 nm colloidal suspension was further investigated due to the well-defined features of its CV trace. As summarized in Figure 5d, variable scan rate measurements showed a strong dependence
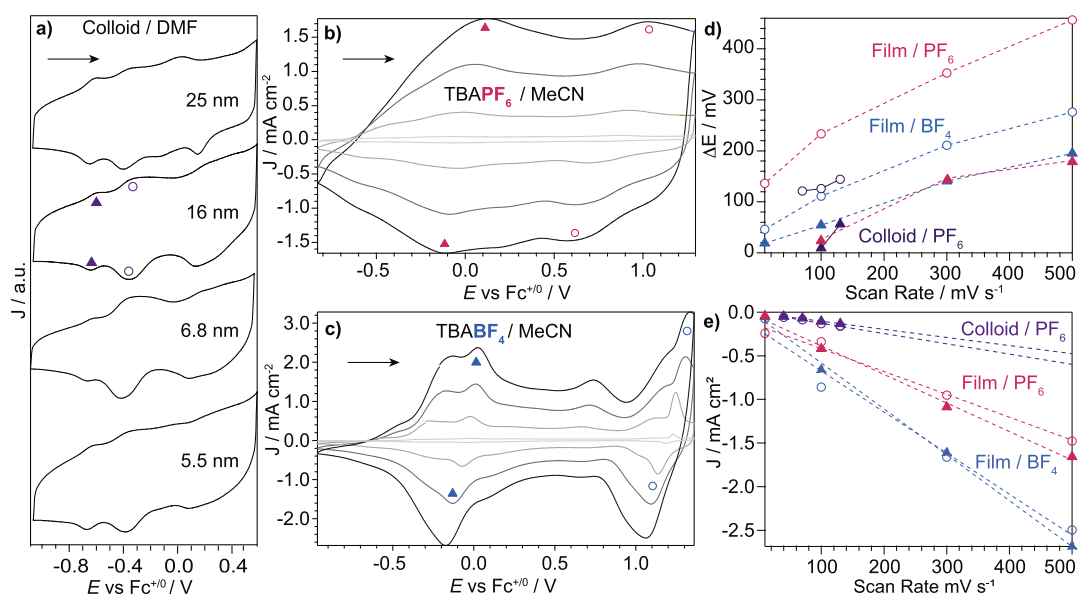
Figure 5. CV of $Fe(TA)_2$ nanoparticles analyzed as colloids or thin films. Initial scan directions are indicated by arrows. (a) CV traces collected at a 130 mV/s scan rate for four particle sizes prepared as colloids in 0.1 M $TBAPF_6$/DMF; current density is normalized to the second faradaic event. Scan rate dependence of 16 nm particles drop-casted onto GC in 0.1 M $TBAPF_6$/MeCN (b) and $TBABF_4$/MeCN (c). Light to dark grayscale traces correspond to 10−500 mV/s. Relevant peaks are marked with filled triangles (first peak analyzed) or open circles (second peak analyzed) in all panels. (d) Peak-to-peak separation with respect to the scan rate. (e) Peak current with respect to the scan rate for two reduction peaks in each of the 16 nm particle CVs. Dashed lines correspond to linear fits.

of the peak-to-peak separation ΔE for the lowest-potential redox event at around −0.61 V (purple closed triangles), ranging from 9.2 mV at 100 mV/s to 56 mV at 130 mV/s, while the second event, centered at −0.29 V (purple open circles), showed less reversibility, with ΔE of 126 mV at 100 mV/s to 144 mV at 130 mV/s (Figure 5d), while ΔE for the highest-potential feature, centered around 0.13 V, could not be resolved.

To investigate the origin of these redox events and to demonstrate that the solution processability of colloidal $Fe(TA)_2$ nanoparticles will facilitate their use in MOF-based electrochemical devices, 16 nm $Fe(TA)_2$ particles were drop-casted onto the surface of glassy carbon (GC) electrodes. Figure 5b shows the variable scan rate CVs of the particle films in 0.1 M $TBAPF_6$/MeCN. Despite the difference in the solvent, which was chosen to discourage particle delamination, the CV traces resemble those of the free-standing colloids in Figure 5a. Because of the small pore size of $Fe(TA)_2$, we hypothesized that the broad waves of the voltammetric response reflect the hindered ability of the bulky PF_6^- anion to diffuse through the material. Therefore, these experiments were repeated on particle films using $TBABF_4$, as previous computational work had shown that the BF_4 anion was just below the pore size of the MOF.[14] In contrast to voltammetry with $TBAPF_6$, the use of $TBABF_4$ causes all peaks to sharpen and induces new voltammetric responses, most notably a sharp, reversible feature at 1.2 V (Figure 5c). For direct quantitative comparison, we investigated two well-defined features from each set of electrolyte experiments, as indicated by open circles and shaded triangles throughout Figure 5. Figure 5d shows that in both electrolyte media, ΔE is always smaller for the lower-potential event, supporting the assignment of this peak to a surface $Fe^{2+/3+}$ species, which benefits from both better ion pairing and faster kinetics of ion diffusion. Additionally, the second event (pink open circles) for a film in $TBAPF_6$ shows the largest ΔE among all conditions, including

the colloidal suspension in $TBAPF_6$/DMF (purple open circles). Interestingly, as shown in Figure 5e, the peak current for the events in all experiments exhibits a linear dependence with respect to the scan rate. Therefore, even if the particles are employed as colloids, the redox events are adsorption-controlled.[42]

To precisely quantify the role of ions in the redox chemistry of $Fe(TA)_2$ particles, we employed quartz crystal microbalance (QCM) electrodes.[43] Spin-coating 16 nm particles onto the QCMs yielded uniform multi-layer nanoparticle films (Figure S27), which allowed us to measure their voltammetric responses and simultaneous mass changes in either $TBAPF_6$ or $TBABF_4$ environments. The frequency of the quartz crystal oscillation is sensitive to mass changes at the crystal surface, allowing monitoring of film loading and ion flux while the potential is scanned. Figure 6a,b shows both the CV traces and the number of moles of anion adsorbed to the particles based on the mass change of the QCM electrode, using the Sauerbrey equation[43] and assuming that all mass change is due to unsolvated PF_6^- and BF_4^- anions. Once again, the redox waves of the sample analyzed with $TBAPF_6$ exhibit broad features in comparison to the same-sized nanoparticles in $TBABF_4$ (Figures 6 and S24). Additionally, substantially more current passes to the particles in the presence of $TBABF_4$. Charge integration shows nearly seven-fold enhancement when assuming all current arises from Faradaic events rather than capacitive charging, with stoichiometric oxidation of nearly all Fe sites, that is, e^-/Fe = ~0.9 when using $TBABF_4$, whereas $TBAPF_6$ yields only e^-/Fe = ~0.3. This comparison suggests that more Fe sites are electrochemically accessible in the $TBABF_4$ experiment, which we attribute mainly to the ability of the smaller anions to diffuse through the porous MOF particles, while bulky PF_6^- anions merely collect at the nanoparticle surface. This result contrasts with studies of ion diffusion in MOFs with large pores, wherein ion pairing hinders small ions to a greater degree than larger ions.[44] A
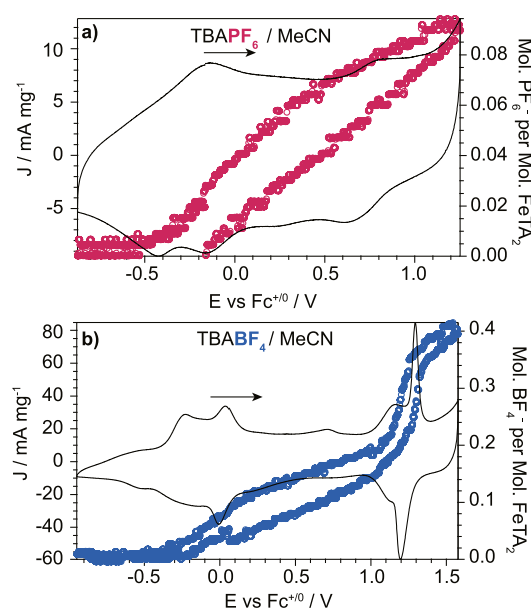
Figure 6. CV with superimposed QCM data of Fe(TA)$_2$ nanoparticles. Initial scan directions are indicated by arrows. CV traces collected at 100 mV/s with a Pt QCM electrode for 16 nm particles in TBAPF$_6$/MeCN (a) and TBABF$_4$. (b) Colored open circles refer to the right axis, moles of anions with respect to moles of Fe(TA)$_2$ on the QCMs.

further contribution may be differences in film thickness and morphology, although films were homogenous for both cases (Figure S27 and Table S7). The mass of the particle films increases in both experiments with oxidizing potentials, as expected for incorporation of charge-balancing anions, but far more anions are incorporated when using the smaller BF$_4^-$ ions. Approximately four times as many moles of BF$_4^-$ adsorb compared to PF$_6^-$, yielding PF$_6$/Fe = 0.1 and BF$_4$/Fe = 0.4 (Table S7). We expect that surface ions provide additional charge-balancing anions needed for stoichiometric oxidation of all Fe sites. Comparing mass changes to redox waves at a given potential provides further insights into the nature of the redox chemistry. Most notably, the coincidence of a sharp increase in mass and current at ~1.2 V strongly suggests that this redox event corresponds to ion-coupled charge transport to interior Fe sites enabled by the smaller size of the BF$_4^-$ anion in comparison to the gradual mass changes and broad redox waves of the TBAPF$_6$ experiments. None of the other features in the CV traces are obviously associated with an increase in mass; rather, in TBAPF$_6$ and at low potentials in TBABF$_4$, the mass increases gradually as the cell is scanned oxidatively. A gradual increase in mass therefore indicates that for these features, ions are collected at the particle surface rather than diffusing through the pores. The observation of several voltammetric features spanning a wide potential window is surprising; however, it is expected that surface species would be oxidized at a lower potential than internal iron sites that require significant ion intercalation. These data stand in stark contrast to two prior reports of bulk Fe(TA)$_2$ cyclic voltammetry. In one study, scanning the bulk material in an air-free environment in LiBF$_4$/propylene carbonate showed a single redox feature at a high potential, assigned to Fe$^{2+/3+}$.[14] In the other report, the material was synthesized under aerobic conditions and scanned in 0.1 M KOH, showing several redox events assigned to varying Fe surface species.[45] Here, we assign

the sharp reversible event at ~1.2 V in TBABF$_4$ to Fe$^{2+/3+}$, while broad events at a lower potential in either electrolyte are assigned to a combination of capacitive charging and surface Fe$^{2+/3+}$ species. CV of the 1,2,3-triazole linker in 0.1 M TBAPF$_6$/DMF reveals a chemically irreversible event at 0.31 V versus Fc$^{+/0}$ (Figure S23), supporting the assignment of redox waves to Fe$^{2+/3+}$. Although ion intercalation and ion pairing are frequently invoked to understand MOF redox chemistry, charge storage, and sensing, these data represent some of the only direct measurements of ion intercalation processes by employing QCM electrodes.[44,46] They also show that nanosizing MOFs can improve the availability of redox-active sites, thus lowering redox potentials through improved ion pairing, a key insight into designing electronic MOF devices.

Thin-film fabrication and solid-state measurements are enabled by the long-term colloidal stability and solution processability of Fe(TA)$_2$ nanoparticles. Doctor blading high-concentration suspensions onto glass slides afforded uniform films with smooth surfaces, as shown in the cross-sectional FIB-SEM images in Figure 7. Additional SEM images and
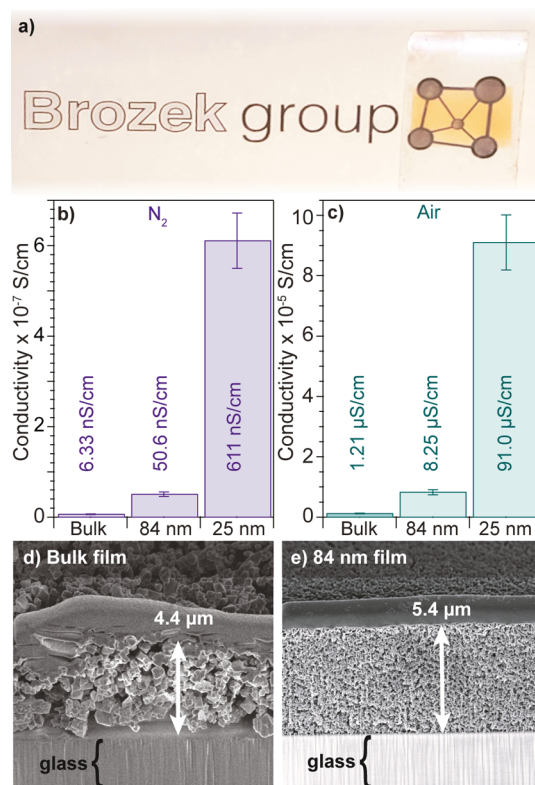
Figure 7. Charge transport measurements of Fe(TA)$_2$ nanoparticle thin films. (a) Photograph of a thin film prepared under N$_2$ by doctor blading 84 nm nanoparticles. (b) van der Pauw DC conductivity values of three Fe(TA)$_2$ thin films under N$_2$ and (c) after three days of air exposure. An error is derived from the ratio between the probe width and the sample width. (d) FIB-SEM image of a cross-section of a representative bulk film. (e) FIB-SEM cross-section of a representative 84 nm film showing dense inter-particle packing.

photographs of particle films can be found in the Supporting Information (Figures S28−S31). Figure 7b shows conductivities of thin films under N$_2$ for the three particle sizes: the conductivity increases from 6.33 nS/cm for the bulk sample to 50.6 nA/cm for 84 nm and finally to 611 nS/cm for a film comprising 25 nm particles. A previous report of bulk Fe(TA)$_2$

measured values of 0.1 nS/cm for a sample kept air-free.[14] Although the values herein are higher, the samples still lack oxidation, as even the smallest particles (5.5 nm) handled air-free do not show Fe^{3+} by Mössbauer spectroscopy (Figure S15). After three days of air exposure, the conductivity of the samples increases to 1.21 (bulk), 8.25 (84 nm), and 91.0 μS/cm (25 nm) (Figure 7c). The values collected in the air agree with the first reported value of 77 μS/cm; the bulk value herein is likely lower due to the air exposure time only lasting three days.[11] These measurements suggest a size dependence in the charge transport behavior of $Fe(TA)_2$, with the conductivity increasing as the particle size decreases. While this trend may be unexpected due to smaller particles introducing more grain boundaries, the cross-sectional SEM images indicate that nanoparticles exhibit denser inter-particle packing in comparison to the bulk material (Figure 6). Hence, despite the largest grain size, the overall conductivity of the bulk sample still suffers in comparison to well-packed nanoparticles. After air exposure, the conductivity of all samples increases by 2 to 3 orders of magnitude, most likely due to oxidation and the creation of mixed valency. Mössbauer data show that samples allowed to oxidize in air contain varying amounts of Fe^{3+}, but the degree of oxidation does not depend on the particle size (Figure S16). Therefore, the main cause of size dependence in the conductivity values arises from efficient particle packing. These results imply that grain boundaries in $Fe(TA)_2$ may present relatively shallow barriers to charge transport. Notably, in polycrystalline organic semiconductor films, smaller grain size does not always decrease conductivity; transport in such systems depends extensively on the microstructure and grain boundary site energy.[47−49] Further investigations are ongoing into the charge transport mechanisms of $Fe(TA)_2$ nanoparticles, including the dependence on size, redox state, and guest−host interactions for technologies ranging from charge storage to electrochemical sensing.

CONCLUSIONS

In summary, conductive $Fe(TA)_2$ nanoparticles can be prepared reproducibly with excellent colloidal stability. The solution processability of this unprecedented class of semiconductor nanocrystals enables solution-state spectroscopy and electrochemistry, whereas MOF characterization typically requires solid-state techniques. These measurements reveal an unexpected size dependence on the optical transitions and enable the first analysis of MOF extinction coefficients, which scale with the particle size. $Fe(TA)_2$ particles can be probed by colloidal and thin-film voltammetry, revealing redox chemistry sensitive to ion pairing and intercalation effects within the porous materials. Finally, we demonstrated that the particles can be easily processed into thin films for charge transport measurements that reveal increased conductivity compared to the bulk material.

EXPERIMENTAL METHODS

Synthesis of Fe(TA)₂ Nanoparticles. Controlling the size of iron triazolate nanoparticles was achieved by changing the amount of 1-mIm added to the synthesis. In a N_2 glovebox, 1-mIm was added to a solution of anhydrous iron(II) chloride in DMF (0.805 mmol, 0.0575 M, 14 mL). The amount of 1-mIm varied from 3.5 μL (0.044 mmol, 0.055 equiv) to 700 μL (8.78 mmol, 10.9 equiv); all equivalents are with respect to iron(II) chloride. Syntheses performed with 5-bromo-1-methylimidazole and 1-benzyl-2-methylimidazole were also performed with these equivalents. Initial exploratory synthesis, conducted

with 1-methylimdazole, nBA, and sodium formate, was performed with 1 equiv (1.15 mmol). Under stirring, 1,2,3-triazole (2.42 mmol, 140 μL, 3 equiv) was added to the reaction solution. Vials were capped and sealed with electrical tape and then placed in an aluminum block pre-heated to 120 °C. The solutions were stirred for 1.5 h, after which they were immediately centrifuged and washed twice with DMF.

PXRD Measurements and Analysis. PXRD data were collected in the air using Bragg−Brentano geometry with a step size of 0.02° in the range of 3.5−35° 2θ with a Bruker D2 Phaser. A variable detector opening was used to reduce air scattering at low angles. Patterns were matched to the low-spin $Fe(TA)_2$ cif file.[15] Gaussian fitting was performed using the Multipeak 2.0 package in Igor 6.3. Scherrer analysis was performed to determine the crystallite size.

$$\tau = \frac{K\lambda}{\beta \cos \theta}$$

In the Scherrer equation above, τ is the crystallite size, K is the shape factor, λ is the source X-ray wavelength (Cu Kα, 0.154 nm), β is the full-width-at-half-maximum in radians, and θ is the half of the peak position in radians. A shape factor (K) of 1 is used as the particles change shape from octahedral to nearly spherical as the size decreases.

SEM Imaging for Size Analysis. Imaging was performed using a FEI Helios 600i instrument with 3.0−5.0 kV energy and 0.43−0.69 nA current. SEM samples were prepared by drop-casting particle dispersions in DMF onto silicon substrates and drying under N_2 pressure. Particle sizing was performed in ImageJ;[50] over 200 particles were measured using the line tool to determine particle diameter. A Gaussian fit was performed for particle size histograms in Igor Pro 6.3. Dispersity was evaluated by dividing the standard deviation of the fit by the mean particle size.

UV−Vis Experiments and Calculations. All UV−vis data were collected using custom-made air-free quartz cuvettes with a pathlength of 1 cm. Long-range scans (1350−265 nm, 1.0 nm resolution) were used for Gaussian fitting, performed with the Multipeak Fitting 2.0 package in Igor 6.3. For Beer's law experiments, measurements were collected only from 900 to 265 nm with 0.5 nm resolution. The particles were diluted until the maximum absorbance was less than 1 and then further diluted four times. A linear relationship between absorbance and concentration, determined either in formula unit molarity or particle molarity, gave the extinction coefficient; the linear fits can be found in Figure S19. Peak maxima reported in the main text were the absolute maximum of the trace determined without a Gaussian fit; Gaussian fit data are available in Figure S20. The extinction coefficient per particle trend was fitted to a cubic equation in Igor 6.3. The y-intercept was set to zero. For CT1, the pre-factor is 18 013, and for CT2, the pre-factor is 15 100. To determine the oscillator strength, the Gaussian fits for CT1, CT2, and the shoulder of CT2 were used. The following relation gives the oscillator strength as a unitless quantity, where ε_{max} is the extinction at the peak of the band and $\nu_{1/2}$ is the full-width-at-half-maximum of the peak.

$$f = 4.61 \times 10^{-9} \varepsilon_{max} \nu_{1/2}$$

CV Experiments. All electrochemical data were collected either with a Biologic SP200 or a Gamry Interface. For solution-state experiments, CV was collected in DMF with 0.1 M $TBAPF_6$ or $TBABF_4$ as the supporting electrolyte in a standard three-electrode cell with a glassy carbon (GC) working electrode, a silver wire pseudo-reference electrode, and a platinum wire counter electrode. Electrodes were polished immediately before use. The blank CV scans showed no faradaic events within the electrochemical window scanned. Particles were added in aliquots until sufficient peaks appeared at 70 mV/s. The total concentration of particles in these experiments is not known but is estimated to be between 0.01 and 0.05 mg/mL. Data were collected within the window of a few hours, as particles suspended in 0.1 M $TBAPF_6$ for several days were observed to aggregate significantly. Data were collected from −0.325 to 1.325 V against Ag/Ag^+ and then ferrocene was added to act as a

reference. Scans were collected at rates of 10, 40, 70, 100, and 130 mV/s. For experiments with $Fe(TA)_2$ on the working electrode, experiments were conducted in acetonitrile (MeCN) with either $TBAPF_6$ or $TBABF_4$ as the electrolyte. A standard three-electrode cell was used, with the particle-coated GC as the working electrode, silver wire as a pseudo-reference electrode, and carbon cloth as a counter electrode. To prepare the working electrode, particles (0.709 equiv 1-methylimidazole, 16 nm) were suspended in DMF at a concentration of 7.7 mg/mL and then drop-casted (7 μL) onto the polished GC surface. For the bulk material, it was necessary to dilute the dispersion to a concentration of 0.6975 mg/mL. The dispersion was allowed to dry under ambient conditions for a few hours and then placed under vacuum to dry completely. Scans were collected at rates of 10, 100, 300, and 500 mV/s. The bare GC electrode was replaced in the cell, and a blank scan was collected to show that no significant particle delamination occurred. Finally, ferrocene was added as a reference, and a scan was collected using the particle-coated electrode. Current density data are normalized to the area of the bare GC working electrode, as the particle dispersion runs off the edges of the electrode, and as such, the exact amount of material on the electrode is less than the amount drop-casted. For QCM experiments, the PT/Ti-coated 5 MHz AT-cut QCM working electrodes were first soaked in acidic piranha solution for ~5 min, then rinsed copiously with 18.2 MΩ nanopure water, followed by isopropyl alcohol, and lastly dried under N_2 pressure. Suspensions of 16 nm particles in DMF were spin-coated onto the QCM electrodes until a minimum of 4 μg was obtained on the surface. An electrochemical cell was set up with 0.1 M $TBAPF_6$ or $TBABF_4$ in MeCN (80 mL), the QCM as the working electrode, carbon cloth as the counter electrode, and a bare silver wire as a pseudo-reference electrode. Frequency data were collected simultaneously with CV scans using a SRS QCM200 apparatus. The frequency was converted to mass using the Sauerbrey equation below, in which Δf is the experimental change in frequency, C_f is the sensitivity factor (56.6 Hz cm^2 μg^{-1} for 5 MHz AT-cut crystals), and Δm is the change in mass.

$$\Delta f = -C_f \times \Delta m$$

Once the mass change is obtained, the value is converted to moles of anions (PF_6^- or BF_4^-); potential solvation of the anions was not considered. These values are then compared to the total number of moles of $Fe(TA)_2$ deposited onto the microbalance. Additional analysis is included in Table S7.

Preparation of $Fe(TA)_2$ Nanoparticle Thin Films. Glass microscope slides were rinsed copiously with isopropyl alcohol and dried with pressurized nitrogen. Substrates were taped to glass slides with electrical tape (U-Line Listed E50292 590J), and a 200 μL aliquot was used to doctor blade the films. Films were made both in a N_2-filled glovebox and in the air with this method. The concentrations for initial tests were 20 mg/mL, but most were diluted slightly to avoid film cracking. To create the composite film, 5% w/w suspensions of carbon black and poly(vinylidene difluoride) were created in DMF. The suspensions were then added to a concentrated 84 nm particle suspension, and the total volume was diluted to create an overall concentration of 20 mg/mL. The bulk sample film was created by dispersing the bulk powder in DMF and sonicating for 10 min; the film was created directly after the sonication step. Samples were allowed to dry overnight. Samples fabricated in the N_2-filled glovebox were additionally dried under vacuum for at least 1 h.

Conductivity Measurements. The conductivity of the thin films was determined using the van der Pauw method both under N_2 and after air exposure. Silver paint was dotted at the four corners of the thin films, and contact was made with flat copper alligator clips. The resistivity was calculated with the following equation, where t is the film thickness and the two R values are the resistances derived from the slopes of the IV curves of the two different measurement configurations.[51]

$$\rho = \frac{\pi t}{\ln(2)} \frac{(R_{12,34} + R_{23,41})}{2} F$$

Because the thin films are not perfectly square, the correction factor F was found using the following relation, where R_r is the ratio between the two resistivities measured.

$$\frac{R_r - 1}{R_r + 1} = \frac{F}{\ln(2)} A \cosh\left(\frac{\exp\left(\frac{\ln(2)}{F}\right)}{2}\right)$$

Further measurements were conducted using a four-point probe method on films that were doctor bladed under aerobic ambient conditions. Four tungsten carbide probes (distance = 1 mm) were placed on the film close to the center of the film surface. Two separate resistivity measurements were collected, with either forward or reverse bias. To calculate the resistivity of the films, the following relation was used.

$$\rho = \frac{\pi t}{\ln(2)} \left(\frac{V}{I}\right) = 4.532 t \frac{V}{I}$$

In the expression, V/I is the slope of the IV curve and t is the film thickness. Thin films were of sufficient length and thin enough such that further geometric corrections were not needed.[51] For all thin films, film thickness was measured by cross-sectioning the films in a Helios 600i FIB-SEM. Films were capped with carbon prior to FIB-SEM experiments. The stage was set to eucentric focus and tilted to 52°. Regular cross-section cutting was performed with 30 kV and 21 nA current, and then the cross-section was polished by performing a cleaning cross-section at a reduced current of 2.5 nA. Film thickness was then measured with the cross-section measurement tool.

◼ ASSOCIATED CONTENT

ⓢ Supporting Information

The Supporting Information is available free of charge at https://pubs.acs.org/doi/10.1021/jacs.1c10800.

> Additional synthetic experiments and details of $Fe(TA)_2$ nanoparticles, additional characterization on select samples including N_2 sorption, acid digestion ^{1}H NMR, IR, DLS, Mössbauer spectra, additional data for UV−vis measurements and extinction coefficient extraction, additional electrochemical data, photographs and SEM images of nanoparticle thin films (PDF)

◼ AUTHOR INFORMATION

Corresponding Author

Carl K. Brozek − *Department of Chemistry and Biochemistry, Material Science Institute, University of Oregon, Eugene, Oregon 97403, United States;* ⓞ orcid.org/0000-0002-8014-7904; Email: cbrozek@uoregon.edu

Authors

Checkers R. Marshall − *Department of Chemistry and Biochemistry, Material Science Institute, University of Oregon, Eugene, Oregon 97403, United States*

Josh P. Dvorak − *Department of Chemistry and Biochemistry, Material Science Institute, University of Oregon, Eugene, Oregon 97403, United States*

Liam P. Twight − *Department of Chemistry and Biochemistry, Material Science Institute, University of Oregon, Eugene, Oregon 97403, United States*

Lan Chen − *Department of Chemistry and Biochemistry, Material Science Institute, University of Oregon, Eugene, Oregon 97403, United States*

Kentaro Kadota − *Department of Chemistry and Biochemistry, Material Science Institute, University of Oregon, Eugene, Oregon 97403, United States*

Anastasia B. Andreeva − *Department of Chemistry and Biochemistry, Material Science Institute, University of Oregon, Eugene, Oregon 97403, United States*

Alexandra E. Overland − *Department of Chemistry and Biochemistry, Material Science Institute, University of Oregon, Eugene, Oregon 97403, United States*

Thomas Ericson − *Department of Chemistry and Biochemistry, Texas Tech University, Lubbock, Texas 79409, United States*

Anthony F. Cozzolino − *Department of Chemistry and Biochemistry, Texas Tech University, Lubbock, Texas 79409, United States;* ⊙ orcid.org/0000-0002-1100-0829

Complete contact information is available at:
https://pubs.acs.org/10.1021/jacs.1c10800

Notes

The authors declare no competing financial interest.

REFERENCES

(1) Kim, T.-H.; Cho, K.-S.; Lee, E. K.; Lee, S. J.; Chae, J.; Kim, J. W.; Kim, D. H.; Kwon, J.-Y.; Amaratunga, G.; Lee, S. Y.; Choi, B. L.; Kuk, Y.; Kim, J. M.; Kim, K. Full-Colour Quantum Dot Displays Fabricated by Transfer Printing. *Nat. Photonics* **2011**, *5*, 176−182.

(2) Cai, X.; Xie, Z.; Li, D.; Kassymova, M.; Zang, S.-Q.; Jiang, H.-L. Nano-Sized Metal-Organic Frameworks: Synthesis and Applications. *Coord. Chem. Rev.* **2020**, *417*, 213366.

(3) Wuttke, S.; Lismont, M.; Escudero, A.; Rungtaweevoranit, B.; Parak, W. J. Positioning Metal-Organic Framework Nanoparticles within the Context of Drug Delivery − A Comparison with Mesoporous Silica Nanoparticles and Dendrimers. *Biomaterials* **2017**, *123*, 172−183.

(4) Gao, R.; Zhang, G.; Ru, X.; Xu, C.; Li, M.; Lin, R.; Wang, Z. Morphology Control of Metal-Organic Frameworks by Co-Competitive Coordination Strategy for Low-Temperature Selective Catalytic Reduction of NO with NH₃. *J. Solid State Chem.* **2021**, *297*, 122031.

(5) Bonnett, B. L.; Smith, E. D.; De La Garza, M.; Cai, M.; Haag, J. V.; Serrano, J. M.; Cornell, H. D.; Gibbons, B.; Martin, S. M.; Morris, A. J. PCN-222 Metal−Organic Framework Nanoparticles with Tunable Pore Size for Nanocomposite Reverse Osmosis Membranes. *ACS Appl. Mater. Interfaces* **2020**, *12*, 15765−15773.

(6) Mandal, T. N.; Karmakar, A.; Sharma, S.; Ghosh, S. K. Metal-Organic Frameworks (MOFs) as Functional Supramolecular Architectures for Anion Recognition and Sensing. *Chem. Rec.* **2018**, *18*, 154−164.

(7) Qian, Q.; Asinger, P. A.; Lee, M. J.; Han, G.; Mizrahi Rodriguez, K.; Lin, S.; Benedetti, F. M.; Wu, A. X.; Chi, W. S.; Smith, Z. P. MOF-Based Membranes for Gas Separations. *Chem. Rev.* **2020**, *120*, 8161−8266.

(8) Maka, V. K.; Mukhopadhyay, A.; Jindal, S.; Moorthy, J. N. Redox-Reversible 2D Metal−Organic Framework Nanosheets (MONs) Based on the Hydroquinone/Quinone Couple. *Chem.—Eur. J.* **2019**, *25*, 3835−3842.

(9) Marshall, C. R.; Staudhammer, S. A.; Brozek, C. K. Size Control over Metal−Organic Framework Porous Nanocrystals. *Chem. Sci.* **2019**, *10*, 9396−9408.

(10) D'Alessandro, D. M. Exploiting Redox Activity in Metal−Organic Frameworks: Concepts, Trends and Perspectives. *Chem. Commun.* **2016**, *52*, 8957−8971.

(11) Gándara, F.; Uribe-romo, F. J.; Britt, D. K.; Furukawa, H.; Lei, L.; Cheng, R.; Duan, X.; O'Keeffe, M.; Yaghi, O. M. Porous, Conductive Metal-Triazolates and Their Structural Elucidation by The Charge-Flipping Method. *Chem.—Eur. J.* **2012**, *18*, 10595−10601.

(12) Marshall, C. R.; Timmel, E. E.; Staudhammer, S. A.; Brozek, C. K. Experimental Evidence for a General Model of Modulated MOF Nanoparticle Growth. *Chem. Sci.* **2020**, *11*, 11539−11547.

(13) Guo, C.; Zhang, Y.; Guo, Y.; Zhang, L.; Zhang, Y.; Wang, J. A General and Efficient Approach for Tuning the Crystal Morphology of Classical MOFs. *Chem. Commun.* **2018**, *54*, 252−255.

(14) Park, J. G.; Aubrey, M. L.; Oktawiec, J.; Chakarawet, K.; Darago, L. E.; Grandjean, F.; Long, G. J.; Long, J. R. Charge Delocalization and Bulk Electronic Conductivity in the Mixed-Valence Metal−Organic Framework Fe(1,2,3-Triazolate)₂ (BF₄)ₓ. *J. Am. Chem. Soc.* **2018**, *140*, 8526−8534.

(15) Grzywa, M.; Röß-Ohlenroth, R.; Muschielok, C.; Oberhofer, H.; Błachowski, A.; Żukrowski, J.; Vieweg, D.; von Nidda, H.-A. K.; Volkmer, D. Cooperative Large-Hysteresis Spin-Crossover Transition in the Iron(II) Triazolate [Fe(Ta)₂] Metal−Organic Framework. *Inorg. Chem.* **2020**, *59*, 10501−10511.

(16) Díaz-García, M.; Mayoral, Á.; Díaz, I.; Sánchez-Sánchez, M. Nanoscaled M-MOF-74 Materials Prepared at Room Temperature. *Cryst. Growth Des.* **2014**, *14*, 2479−2487.

(17) Xu, X. Controllable Synthesis of Ultra-Small Metal−Organic Framework Nanocrystals Composed of Copper(II) Carboxylates. *Nanoscale* **2016**, *8*, 16725−16732.

(18) Zheng, W.; Hao, X.; Zhao, L.; Sun, W. Controllable Preparation of Nanoscale Metal−Organic Frameworks by Ionic Liquid Microemulsions. *Ind. Eng. Chem. Res.* **2017**, *56*, 5899−5905.

(19) Shimpi, J. R.; Sidhaye, D. S.; Prasad, B. L. V. Digestive Ripening: A Fine Chemical Machining Process on the Nanoscale. *Langmuir* **2017**, *33*, 9491−9507.

(20) Van Vleet, M. J.; Weng, T.; Li, X.; Schmidt, J. R. In Situ, Time-Resolved, and Mechanistic Studies of Metal-Organic Framework Nucleation and Growth. *Chem. Rev.* **2018**, *118* (7), 3681−3721.

(21) Rojas, S.; Carmona, F. J.; Maldonado, C. R.; Horcajada, P.; Hidalgo, T.; Serre, C.; Navarro, J. A. R.; Barea, E. Nanoscaled Zinc Pyrazolate Metal−Organic Frameworks as Drug-Delivery Systems. *Inorg. Chem.* **2016**, *55*, 2650−2663.

(22) Ranft, A.; Betzler, S. B.; Haase, F.; Lotsch, B. V. Additive-Mediated Size Control of MOF Nanoparticles. *CrystEngComm* **2013**, *15*, 9296−9300.

(23) Pan, Y.; Liu, Y.; Zeng, G.; Zhao, L.; Lai, Z. Rapid Synthesis of Zeolitic Imidazolate Framework-8 (ZIF-8) Nanocrystals in an Aqueous System. *Chem. Commun.* **2011**, *47*, 2071.

(24) Cravillon, J.; Münzer, S.; Lohmeier, S.-J.; Feldhoff, A.; Huber, K.; Wiebcke, M. Rapid Room-Temperature Synthesis and Characterization of Nanocrystals of a Prototypical Zeolitic Imidazolate Framework. *Chem. Mater.* **2009**, *21*, 1410−1412.

(25) Wang, S.; Chen, Y.; Wang, S.; Li, P.; Mirkin, C. A.; Farha, O. K. DNA-Functionalized Metal−Organic Framework Nanoparticles for Intracellular Delivery of Proteins. *J. Am. Chem. Soc.* **2019**, *141*, 2215−2219.

(26) Tan, P. C.; Ooi, B. S.; Ahmad, A. L.; Low, S. C. Size Control and Stability Study of Zeolitic Imidazolate Framework-8 to Prepare Mixed Matrix Membrane. *J. Phys. Sci.* **2017**, *28*, 215−226.

(27) Cheng, C.; Zhang, R.; Wang, J.; Zhang, Y.; Wen, C.; Tan, Y.; Yang, M. An Ultrasensitive and Selective Fluorescent Nanosensor Based on Porphyrinic Metal−Organic Framework Nanoparticles for Cu²⁺ Detection. *Analyst* **2020**, *145*, 797−804.

(28) Razavi, S. A. A.; Masoomi, M. Y.; Morsali, A. Stimuli-Responsive Metal−Organic Framework (MOF) with Chemo-Switch-

able Properties for Colorimetric Detection of CHCl$_3$. *Chem.—Eur. J.* **2017**, *23*, 12559−12564.

(29) Wang, J.; Fan, Y.; Lee, H.-w.; Yi, C.; Cheng, C.; Zhao, X.; Yang, M. Ultrasmall Metal−Organic Framework Zn-MOF-74 Nanodots: Size-Controlled Synthesis and Application for Highly Selective Colorimetric Sensing of Iron(III) in Aqueous Solution. *ACS Appl. Nano Mater.* **2018**, *1*, 3747−3753.

(30) Decker, G. E.; Stillman, Z.; Attia, L.; Fromen, C. A.; Bloch, E. D. Controlling Size, Defectiveness, and Fluorescence in Nanoparticle UiO-66 through Water and Ligand Modulation. *Chem. Mater.* **2019**, *31*, 4831−4839.

(31) Sun, L.; Hendon, C. H.; Park, S. S.; Tulchinsky, Y.; Wan, R.; Wang, F.; Walsh, A.; Dincă, M. Is Iron Unique in Promoting Electrical Conductivity in MOFs? *Chem. Sci.* **2017**, *8*, 4450−4457.

(32) Norris, D. J.; Bawendi, M. G. Measurement and Assignment of the Size-Dependent Optical Spectrum in CdSe Quantum Dots. *Phys. Rev. B: Condens. Matter Mater. Phys.* **1996**, *53*, 16338−16346.

(33) Siddiqui, S. A.; Domanov, O.; Schafler, E.; Vejpravova, J.; Shiozawa, H. Synthesis and Size-Dependent Spin Crossover of Coordination Polymer [Fe(Htrz)$_2$(Trz)](BF$_4$). *J. Mater. Chem. C* **2021**, *9*, 1077−1084.

(34) Hauser, A. Intersystem Crossing in the [Fe(Ptz)$_6$](BF$_4$)$_2$ Spin Crossover System (Ptz=1-Propyltetrazole). *J. Chem. Phys.* **1991**, *94*, 2741−2748.

(35) Hauser, A.; Guetlich, P.; Spiering, H. High-Spin → Low-Spin Relaxation Kinetics and Cooperative Effects in the [Fe(Ptz)$_6$](BF$_4$)$_2$ and [Zn$_{1-x}$Fe$_x$(Ptz)$_6$](BF$_4$)$_2$ (Ptz = 1-Propyltetrazole) Spin-Crossover Systems. *Inorg. Chem.* **1986**, *25*, 4245−4248.

(36) Rajh, T.; Chen, L. X.; Lukas, K.; Liu, T.; Thurnauer, M. C.; Tiede, D. M. Surface Restructuring of Nanoparticles: An Efficient Route for Ligand−Metal Oxide Crosstalk. *J. Phys. Chem. B* **2002**, *106*, 10543−10552.

(37) Dai, Q.; Wang, Y.; Li, X.; Zhang, Y.; Pellegrino, D. J.; Zhao, M.; Zou, B.; Seo, J.; Wang, Y.; Yu, W. W. Size-Dependent Composition and Molar Extinction Coefficient of PbSe Semiconductor Nanocrystals. *ACS Nano* **2009**, *3*, 1518−1524.

(38) Liu, X.; Atwater, M.; Wang, J.; Huo, Q. Extinction Coefficient of Gold Nanoparticles with Different Sizes and Different Capping Ligands. *Colloids Surf., B: Biointerfaces* **2007**, *58*, 3−7.

(39) Moreels, I.; Lambert, K.; De Muynck, D.; Vanhaecke, F.; Poelman, D.; Martins, J. C.; Allan, G.; Hens, Z. Composition and Size-Dependent Extinction Coefficient of Colloidal PbSe Quantum Dots. *Chem. Mater.* **2007**, *19*, 6101−6106.

(40) Zhang, Y.; Wang, X.; Ma, M.; Fu, D.; Gu, N.; Lu, Z.; Xu, J.; Xu, L.; Chen, K. Size Dependence of Second-Order Optical Nonlinearity of CdS Nanoparticles Studied by Hyper-Rayleigh Scattering. *J. Colloid Interface Sci.* **2003**, *266*, 377−381.

(41) Mayerhöfer, T. G.; Höfer, S.; Popp, J. Deviations from Beer's Law on the Microscale − Nonadditivity of Absorption Cross Sections. *Phys. Chem. Chem. Phys.* **2019**, *21*, 9793−9801.

(42) Bard, A. J.; Faulkner, L. R. *Electrochemical Methods: Fundamentals and Applications*, 2nd ed.; Wiley: New York, 2001.

(43) Reviakine, I.; Johannsmann, D.; Richter, R. P. Hearing What You Cannot See and Visualizing What You Hear: Interpreting Quartz Crystal Microbalance Data from Solvated Interfaces. *Anal. Chem.* **2011**, *83*, 8838−8848.

(44) Celis-Salazar, P. J.; Cai, M.; Cucinell, C. A.; Ahrenholtz, S. R.; Epley, C. C.; Usov, P. M.; Morris, A. J. Independent Quantification of Electron and Ion Diffusion in Metallocene-Doped Metal−Organic Frameworks Thin Films. *J. Am. Chem. Soc.* **2019**, *141*, 11947−11953.

(45) Huang, Z. H.; Xie, N. H.; Zhang, M.; Xu, B. Q. Nonpyrolyzed Fe−N Coordination-Based Iron Triazolate Framework: An Efficient and Stable Electrocatalyst for Oxygen Reduction Reaction. *ChemSusChem* **2019**, *12*, 200−207.

(46) Okada, K.; Sawai, S.; Ikigaki, K.; Tokudome, Y.; Falcaro, P.; Takahashi, M. Electrochemical Sensing and Catalysis Using Cu$_3$(BTC)$_2$ Coating Electrodes from Cu(OH)$_2$ Films. *CrystEngComm* **2017**, *19*, 4194−4200.

(47) Kobayashi, H.; Tokita, Y. Modeling of Hole Transport across Grain Boundaries in Organic Semiconductors for Mesoscale Simulations. *Appl. Phys. Express* **2015**, *8*, 051602.

(48) Vladimirov, I.; Kühn, M.; Geßner, T.; May, F.; Weitz, R. T. Energy Barriers at Grain Boundaries Dominate Charge Carrier Transport in an Electron-Conductive Organic Semiconductor. *Sci. Rep.* **2018**, *8*, 14868.

(49) Horowitz, G.; Hajlaoui, M. E. Mobility in Polycrystalline Oligothiophene Field-Effect Transistors Dependent on Grain Size. *Adv. Mater.* **2000**, *12*, 1046−1050.

(50) Schneider, C. A.; Rasband, W. S.; Eliceiri, K. W. NIH Image to ImageJ: 25 years of image analysis. *Nat. Methods* **2012**, *9*, 671−675.

(51) Schroder, D. K. *Semiconductor Material and Device Characterization*, 2nd ed.; John Wiley & Sons, Inc.: New York, NY, 1998.

🕮 Recommended by ACS

On-Surface Synthesis: A New Route Realizing Single-Layer Conjugated Metal–Organic Structures

Jing Liu, Nian Lin, *et al.*

FEBRUARY 03, 2022
THE JOURNAL OF PHYSICAL CHEMISTRY LETTERS

READ ☐

Room Temperature Metallic Conductivity in a Metal–Organic Framework Induced by Oxidation

Andrew J. Clough, Smaranda C. Marinescu, *et al.*

SEPTEMBER 25, 2019
JOURNAL OF THE AMERICAN CHEMICAL SOCIETY

READ ☐

Large Single Crystals of Two-Dimensional π-Conjugated Metal–Organic Frameworks via Biphasic Solution-Solid Growth

Dong-Gwang Ha, Marc A. Baldo, *et al.*

DECEMBER 08, 2020
ACS CENTRAL SCIENCE

READ ☐

Exotic Topological Bands and Quantum States in Metal–Organic and Covalent–Organic Frameworks

Wei Jiang, Feng Liu, *et al.*

JANUARY 05, 2021
ACCOUNTS OF CHEMICAL RESEARCH

READ ☐

Get More Suggestions >